# Supporting Information

# Stoichiometry-Controlled $Mo_xW_{1-x}Te_2$ Nanowhiskers: A Novel Electrocatalyst for Pt-free Dye-Sensitized Solar Cells

Roshan Jesus Mathew,[†,‡,§,□] Chuan-Pei Lee,[⊥,□] Chi-Ang Tseng,[∥] Pradyumna Kumar Chand,[∥] Yi-June Huang,[#] Han-Ting Chen,[#] Kuo-Chuan Ho,[#] Aswin kumar Anbalagan,[†] Chih-Hao Lee,[†] and Yit-Tsong Chen[*,§,∥]

[†] Department of Engineering and System Science, National Tsing-Hua University, No. 101, Section 2, Kuang-Fu Road, Hsinchu 30013, Taiwan.

[‡] Nano-Science and Technology Program, Taiwan International Graduate Program, Academia Sinica, No. 128, Section 2, Academia Rd, Nangang, Taipei, 11529, Taiwan.

[§] Institute of Atomic and Molecular Sciences, Academia Sinica, No. 1, Section 4, Roosevelt Road, Taipei 10617, Taiwan.

[⊥] Department of Applied Physics and Chemistry, University of Taipei, Taipei 10048, Taiwan.

[∥] Department of Chemistry, National Taiwan University, No. 1, Section 4, Roosevelt Road, Taipei 10617, Taiwan.

[#] Department of Chemical Engineering, National Taiwan University, Taipei 10617, Taiwan.

[□] These authors contributed equally to this work.

*E-mail: ytcchem@ntu.edu.tw

**Section S1. Growth of $Mo_xW_{1-x}Te_2$ Nanowhiskers in APCVD Reactions**

The synthesis of $Mo_xW_{1-x}Te_2$ nanowhiskers in APCVD reactions involves three steps: (i) the formation of metal oxychloride at 280 $^oC$, (ii) the decomposition of metal oxychloride and the reduction of metal oxides at 350 $^oC$, and (iii) the tellurization at 760 $^oC$. The temperature profiles during the APCVD synthesis are presented in **Figure S1**. The growth of $Mo_xW_{1-x}Te_2$ nanowhiskers is highly reproducible.

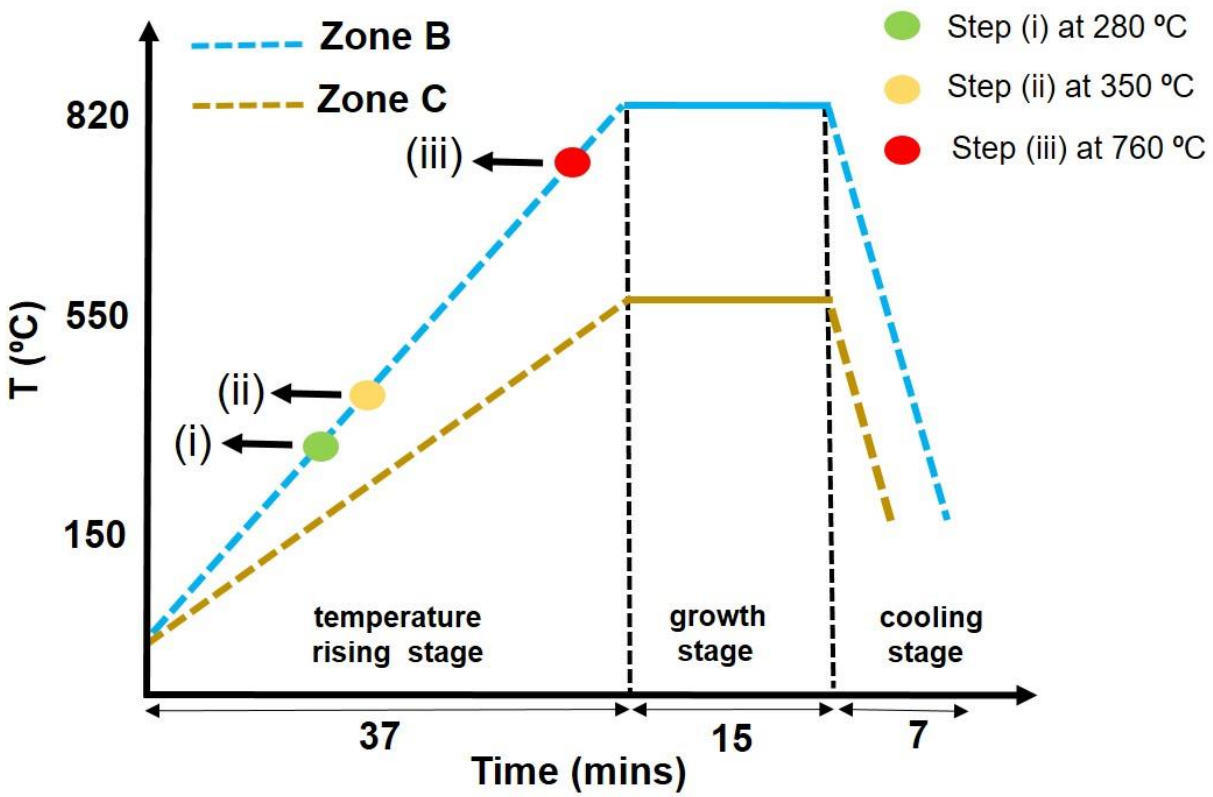


**Figure S1.** The temporal temperature profiles for the synthesis of $Mo_xW_{1-x}Te_2$ nanowhiskers conducted in APCVD reactions.

**Section S2. Scanning Electron Microscopy (SEM)**

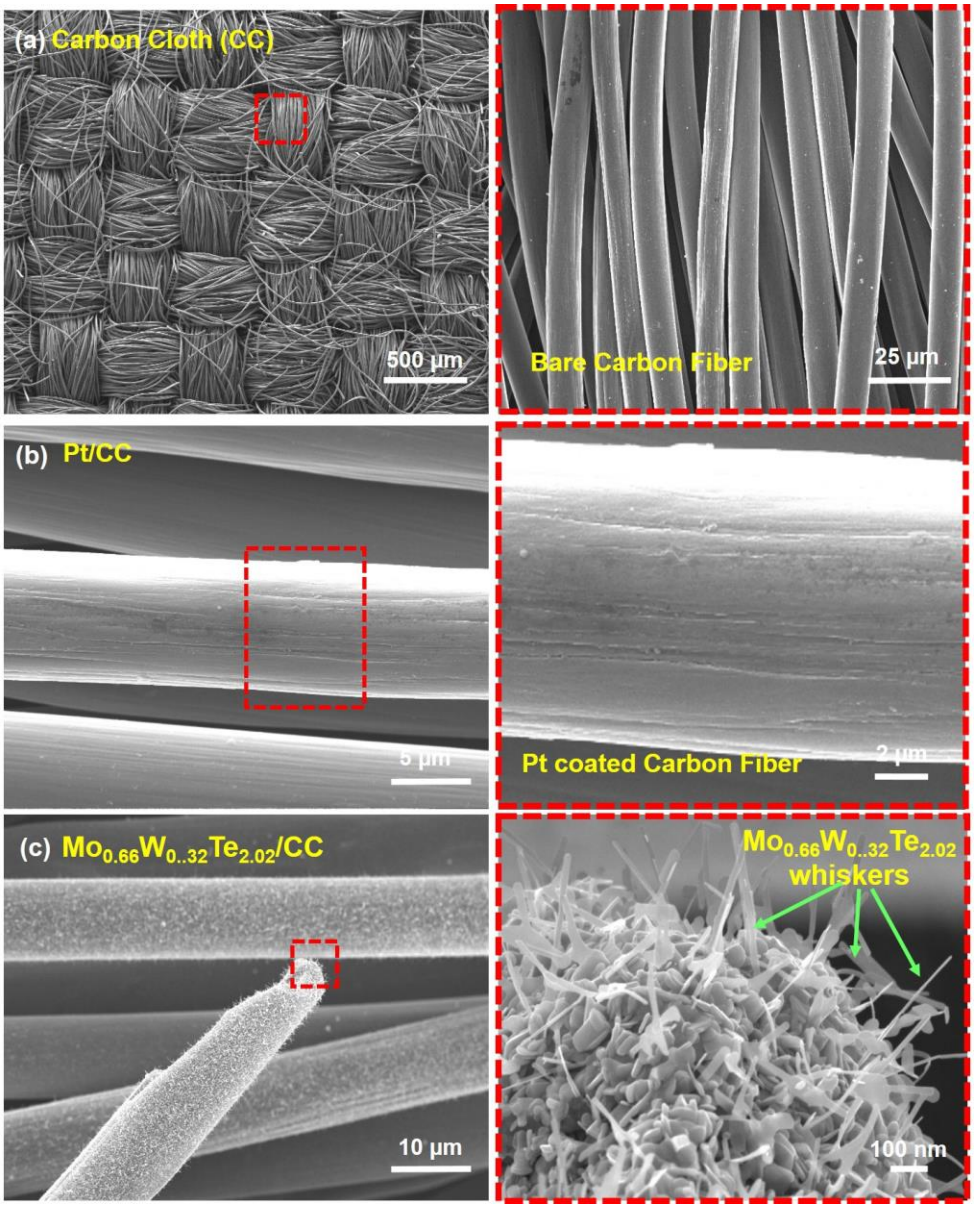


**Figure S2.** SEM images show (a) the bare carbon cloth (CC) surface, (b) carbon fibers coated with platinum (Pt/CC) used as a reference electrode, and (c) carbon fibers decorated with randomly oriented vertical $Mo_xW_{1-x}Te_2$ nanowhiskers. In the left panels, the regions marked by red dashed squares are magnified in the right panel for detailed morphologies.

## Section S3. X-ray Photoelectron Spectroscopy (XPS)

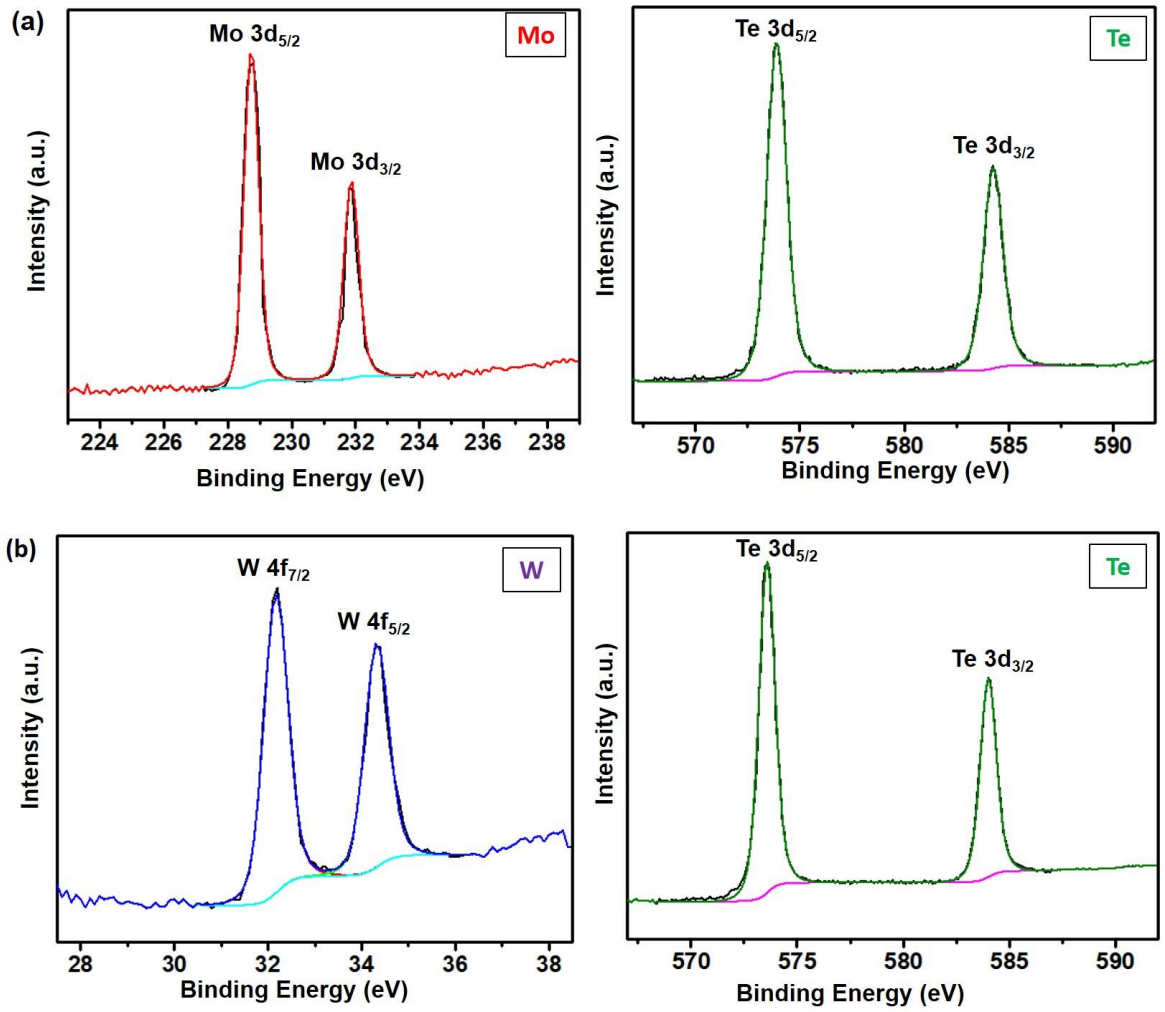


**Figure S3.** The observed XPS spectra of (a) $MoTe_2$ nanowhiskers and (b) $WTe_2$ nanowhiskers exhibit the Mo 3d, W 4f, and Te 3d levels, in which the doublets are caused by the spin-orbit couplings. (a) For $MoTe_2$ nanowhiskers, the binding energies include Mo: $3d_{5/2}$ (228.69 eV) and $3d_{3/2}$ (231.85 eV) and Te: $3d_{5/2}$ (573.60 eV) and $3d_{3/2}$ (583.96 eV). (b) For $WTe_2$ nanowhiskers, the binding energies observed are W: $4f_{7/2}$ (32.46 eV) and $4f_{5/2}$ (34.65 eV) and Te: $3d_{5/2}$ (573.90 eV) and $3d_{3/2}$ (584.29 eV).

**Section S4. High-Resolution Transmission Electron Microscopy (HR-TEM)**

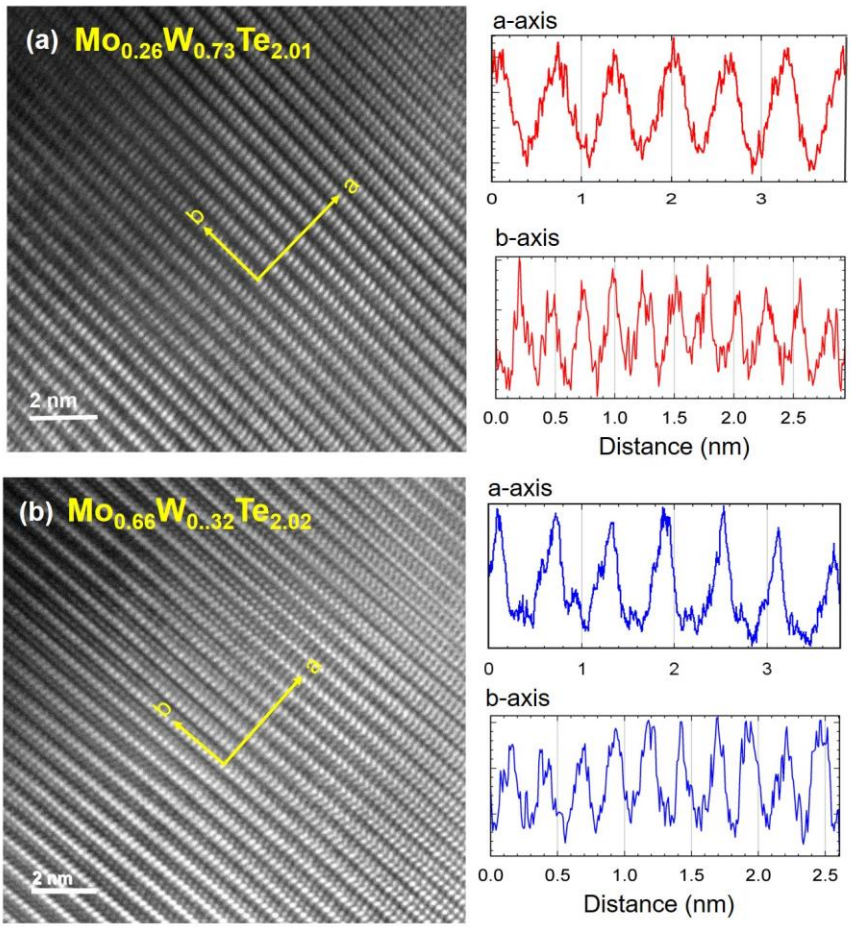


**Figure S4**. In the left column, the HR-TEM images of (a) $T_d$-$Mo_{0.26}W_{0.73}Te_{2.01}$ and (b) *1T'*- & $T_d$-$Mo_{0.66}W_{0.32}Te_{2.02}$ nanowhiskers are presented. In the right column, the plot profiles shown in the panels reveal the lattice spacings along the a-axis (top) and b-axis (bottom) of the crystalline structures in the HR-TEM images.

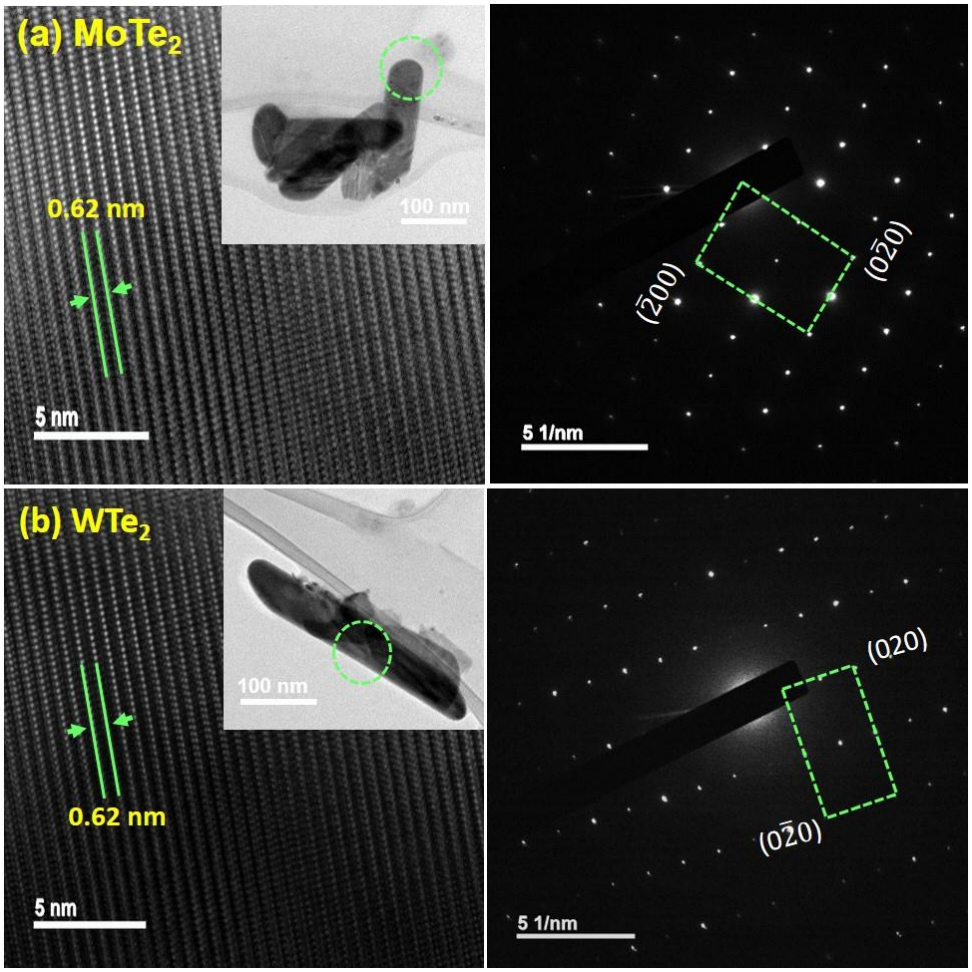


**Figure S5.** The HR-TEM images and SAED patterns of (a) a $MoTe_2$ nanowhisker and (b) a $WTe_2$ nanowhisker were obtained. A TEM image of the single nanowhisker for taking the HR-TEM and SAED examinations is presented in the inset, where the spot marked by a green circle was selected for the HR-TEM and SAED measurements.

## Section S5. Electrochemical Experiments

### 1. Materials and Chemicals

Lithium iodide (LiI, synthetical grade) and iodine ($I_2$, synthetical grade) were obtained from Merck. Acetone (99+%), tert-butyl alcohol (tBA, 96%), guanidine thiocyanate (GuSCN, 99+%), and 4-tert-butylpyridine (TBP, 96%) were bought from Acros. Titanium(IV) tetraisopropoxide (TTIP, >98%), lithium perchlorate ($LiClO_4$, ≥98.0%), ethanol (EtOH, absolute), isopropyl alcohol (IPA, 99.5%), sulfuric acid ($H_2SO_4$, 95–97%), and 2-methoxyethanol (99.95%) were received from Sigma-Aldrich. Acetonitrile (ACN, 99.99%) was procured from J. T. Baker. 1,2-dimethyl-3-propylimidazolium iodide (DMPII) and cis-diisothiocyanato-bis (2,2'-bipyridyl-4,4'-dicarboxylato) ruthenium(II) bis(tetra-butylammonium) (N719 dye) were purchased from Solaronix (S.A., Aubonne, Switzerland). Carbon cloth (CC, W0S1002, thickness: 0.36 mm, basic weight: 120 g $cm^{-2}$, sheet resistance: 0.63 Ω $sq.^{-1}$) was obtained from CeTech Co., Ltd., Taiwan.

### 2. Preparation of Counter Electrodes and Electrochemical Measurements

The as-grown $Mo_xW_{1-x}Te_2$/CCs with various stoichiometric ratios were used as different counter electrodes (CEs) in a DSSC for tests. Meanwhile, with a direct current (DC) sputtering method, a Pt catalytic layer deposited on a cleaned CC substrate was used as a standard CE (represented by a sputtered Pt/CC).

The surface of the DSSC was covered by a mask, leaving a light-illuminating area of 0.16 $cm^2$, and then illuminated by a class-A quality solar simulator (XES-301S, AM 1.5G, SAN-EI ELECTRIC CO., LTD.) with the light intensity of 100 mW $cm^{-2}$. Incident light intensity (100 mW $cm^{-2}$) was calibrated with a standard Si cell (PECSI01, Peccell Technologies, Inc.). Photoelectrochemical characteristics of the DSSC were recorded with a potentiostat/galvanostat

(PGSTAT 30, Autolab, Eco-Chemie, Netherlands). The incident photon-to-electron conversion efficiency (IPCE) curves were obtained at the short-circuit condition. The light source was a class-A quality solar simulator (PEC-L11, AM1.5G, Peccell Technologies, Inc.) and the light was focused through a monochromator (74100, Oriel Instrument) onto the photovoltaic cell. Then, the IPCE ($\lambda$) can be calculated by using the equation, IPCE ($\lambda$) = 1240 ($J_{SC}/\lambda\varphi$), in which $\lambda$ is the wavelength, $J_{SC}$ is the short-circuit photocurrent density (mA $cm^{-2}$) recorded with a potentiostat/galvanostat, and $\varphi$ is the incident radiative flux (W $m^{-2}$) measured with an optical detector (818-SL, Newport) and a power meter (1916-R, Newport).

CV was performed to investigate the electrocatalytic abilities of the tested CEs. The CV was carried out with a three-electrode electrochemical system (a close system) using one of the tested samples (i.e., bare CC, $Mo_xW_{1-x}Te_2$/CC, and a sputtered Pt/CC) as the working electrode, a Pt foil as the CE, and a $Ag/Ag^+$ electrode as the reference electrode in an acetonitrile (ACN) solution, containing 10 mM $I^-$, 1 mM $I_2$, and 0.1 M $LiClO_4$.

Electrochemical properties of the tested CEs were also quantified by Tafel polarization curves (Tafel curves) and EIS, where a symmetric cell, consisting of the same catalytic film on both anode and cathode, was used for these measurements. The data were recorded by the abovementioned potentiostat/galvanostat equipped with a FRA2 module. The electrolyte, containing 0.1 M LiI, 0.6 M DMPII, 0.05 M $I_2$, and 0.5 M TBP in 3-methoxypropionitrile (MPN)/ acetonitrile (ACN) (volume ratio of 1/1), was used for the Tafel analysis (with a scan rate of 50 mV $s^{-1}$) and EIS measurements. Under the open-circuit condition, the EIS analysis was performed between 10 mHz and 65 kHz with an AC amplitude of ±10 mV.

**Section S6. Comparison of Electrocatalytic Performance**

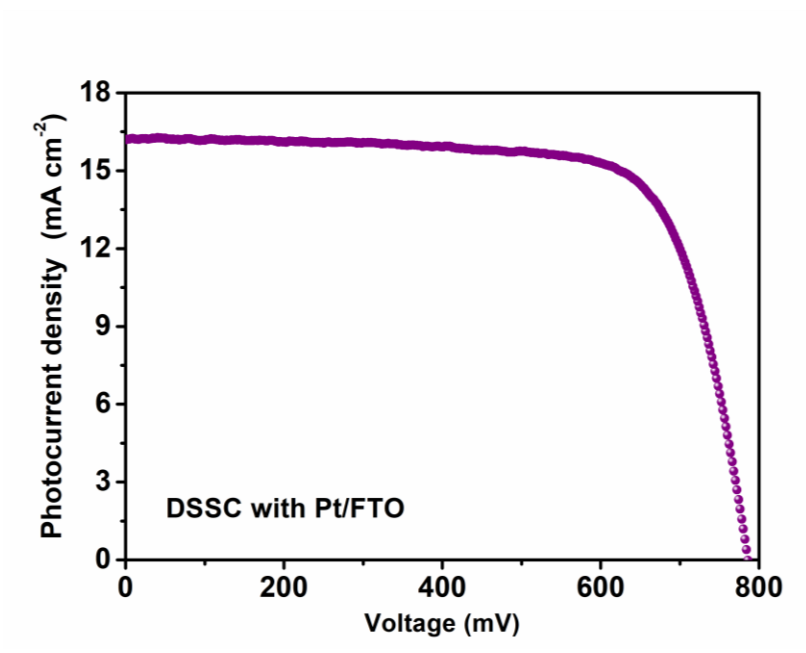


**Figure S6.** The photocurrent density-voltage (*J*–*V*) measurement of a DSSC with a Pt/FTO CE was conducted under AM 1.5G illumination at 100 mW $cm^{-2}$.

**Table S1.** The photovoltaic parameters of a Pt/FTO counter electrode

| Counter Electrode | $\eta$ (%) | $V_{oc}$ (mV) | $J_{sc}$ (mA $cm^{-2}$) | FF |
|---|---|---|---|---|
| Pt/FTO | 9.43 | 784 | 16.21 | 0.74 |

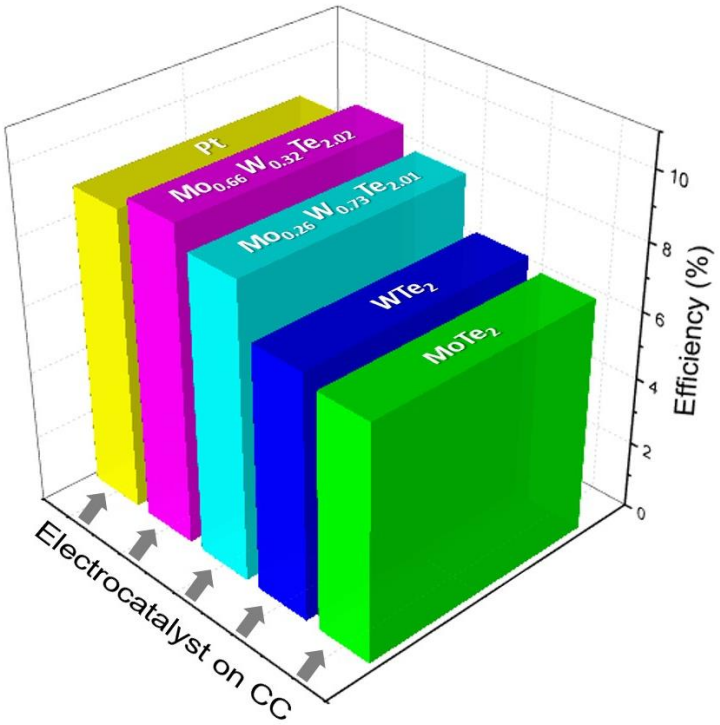


**Figure S7.** The electrocatalytic efficiencies of different stoichiometric $Mo_xW_{1-x}Te_2$/CCs used as CEs in a DSSC are listed for comparison.

**Section S7. Reproducibility Test**

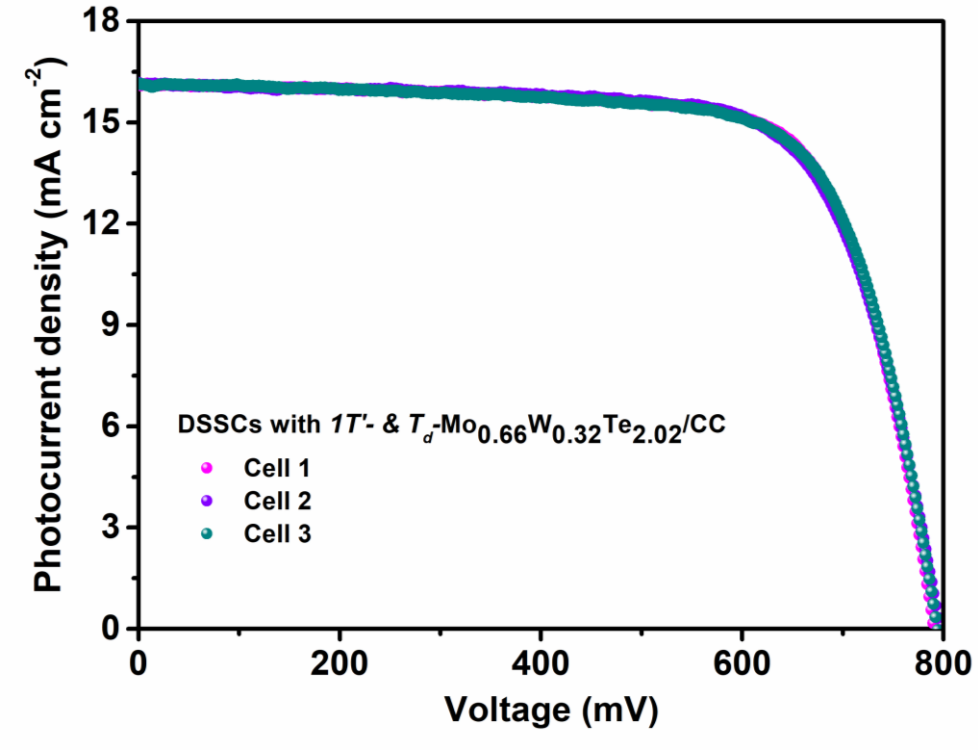


**Figure S8.** The photocurrent density-voltage (*J–V*) measurements of three different *1T'*- & $T_d$-$Mo_{0.66}W_{0.32}Te_{2.02}$/CC CE-based DSSCs were conducted under AM 1.5G illumination at 100 mW $cm^{-2}$ to demonstrate the reproducibility of the material under study.

**Table S2.** The reproducibility test of *1T'*- & $T_d$-$Mo_{0.66}W_{0.32}Te_{2.02}$/CC CE-based DSSCs

| *1T'*- & $T_d$-$Mo_{0.66}W_{0.32}Te_{2.02}$/CC CE-based DSSCs | $\eta$ (%) | $V_{oc}$ (mV) | $J_{sc}$ (mA $cm^{-2}$) | *FF* |
|---|---|---|---|---|
| Cell 1 | 9.38 | 790 | 16.13 | 0.74 |
| Cell 2 | 9.28 | 794 | 16.15 | 0.72 |
| Cell 3 | 9.33 | 792 | 16.14 | 0.73 |
| Average | 9.33 ± 0.05 | 792 ± 2 | 16.14 ± 0.01 | 0.73 ± 0.01 |

## Section S8. Long-Term Stability Tests

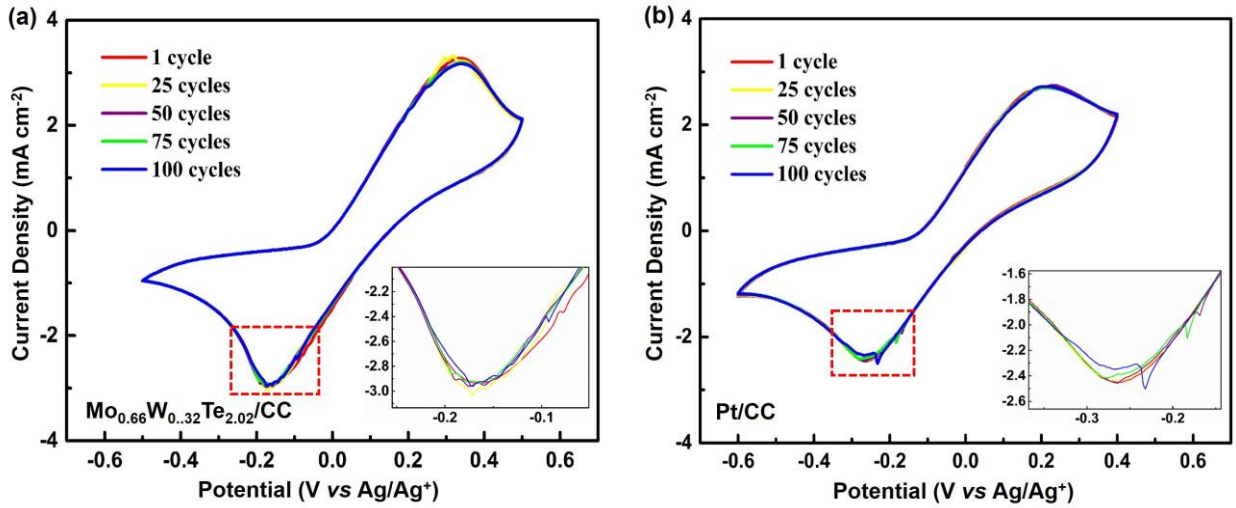


**Figure S9.** The stability tests of the CEs fabricated with (a) *1T'*- & $T_d$-$Mo_{0.66}W_{0.32}Te_{2.02}$/CC and (b) Pt/CC were conducted by continuous 100-cycle CV measurements in the $I^-/I_3^-$ redox reaction. The regions marked by red dashed squares are magnified in the insets.

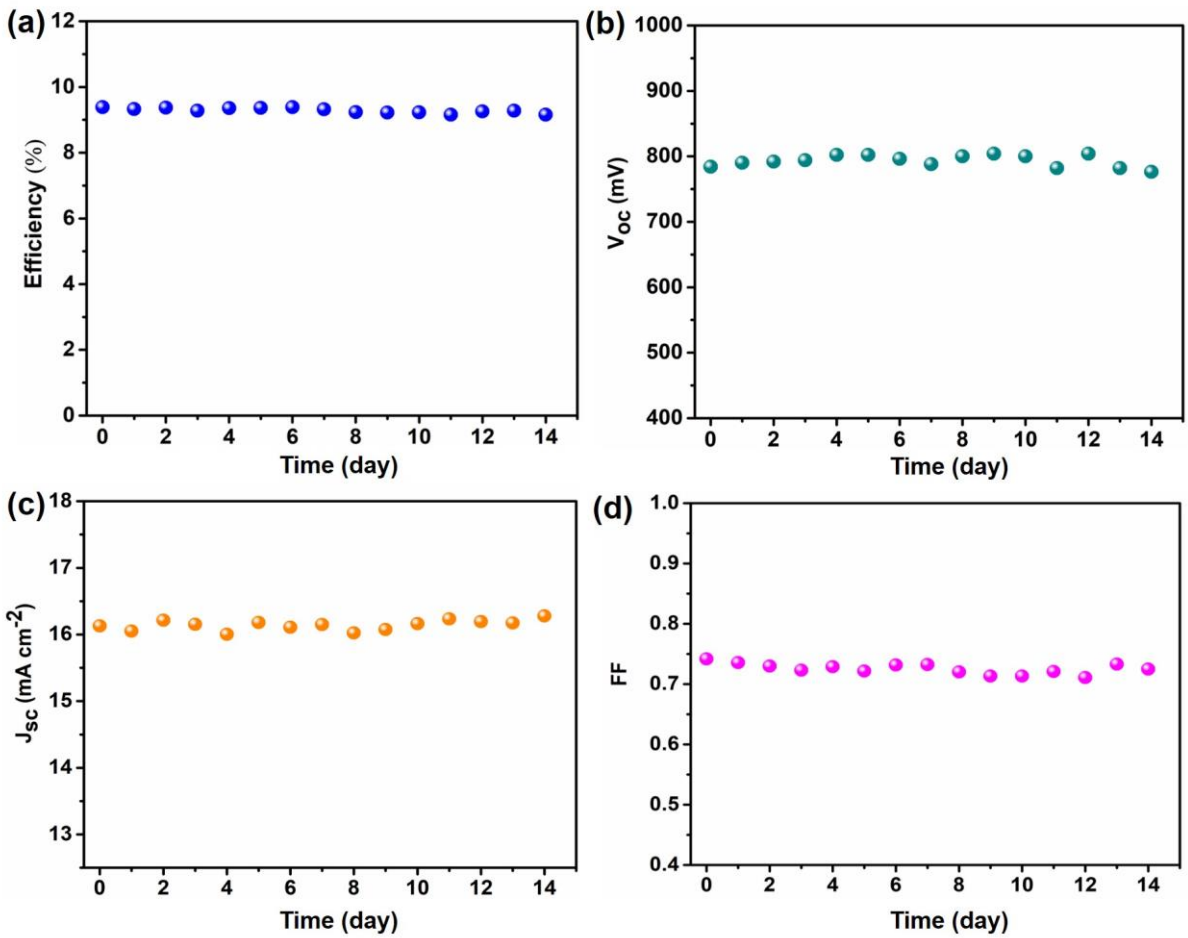


**Figure S10.** The long-term stability of the DSSC fabricated with a *1T'*- & $T_d$-$Mo_{0.66}W_{0.32}Te_{2.02}$/CC CE was tested for 15 days to demonstrate the stability of the photovoltaic parameters of (a) efficiency ($\eta$), (b) open-circuit voltage ($V_{oc}$), (c) short-circuit photocurrent density ($J_{sc}$), and (d) fill factor (*FF*). In this test, the cell was sealed simultaneously with Surlyn and epoxy glue. The cell efficiency was measured once per day after storing the cell in a dark condition at room temperature.

**Section S9. Comparison of Photovoltaic Parameters**

**Table S3.** The measured photovoltaic parameters of the DSSCs with various TMDs-based CEs

| **Counter Electrodes** | $J_{sc}$ (mAcm$^{-2}$ ) | $V_{oc}$ (V) | *FF* (%) | $R_{ct}$ ($\Omega$ cm$^2$) | $\eta$ (%) | **Ref.** |
|---|---|---|---|---|---|---|
| $MoS_2$/NGr | 15.36 | 0.77 | 66 | 16.73 | 7.82 | S1 |
| $WS_2$/MWCNTs | 13.63 | 0.75 | 72 | 2.49 | 7.36 | S2 |
| $TiS_2$/graphene hybrid | 17.76 | 0.72 | 68.5 | 0.63 | 8.80 | S3 |
| $NiS_2$/RGO | 16.55 | 0.749 | 69 | 2.9 | 8.55 | S4 |
| $FeS_2$ | 15.20 | 0.79 | 65 | - | 7.97 | S5 |
| $CoS_2$ | 14.62 | 0.71 | 64 | 7.21 | 6.78 | S6 |
| $SnS_2$/C | 17.47 | 0.745 | 61.9 | 5.2 | 8.06 | S7 |
| $MoSe_2$ | 16.71 | 0.746 | 72.2 | 1.39 | 9.00 | S8 |
| $NbSe_2$/C | 15.58 | 0.77 | 65 | 3.52 | 7.80 | S9 |
| $WSe_2$ | 15.50 | 0.73 | 66 | 0.78 | 7.48 | S10 |
| $TaSe_2$ | 15.81 | 0.73 | 64 | 1.89 | 7.32 | S10 |
| $NiSe_2$ | 15.94 | 0.734 | 74.3 | 0.81 | 8.69 | S11 |
| $FeSe_2$ | 16.14 | 0.744 | 70 | 0.49 | 8.39 | S12 |
| $CoSe_2$/C | 18.16 | 0.76 | 71 | - | 9.87 | S13 |
| $Bi_2Se_3$/graphene | 16.36 | 0.75 | 57 | - | 7.09 | S14 |

| | | | | | | |
|---|---|---|---|---|---|---|
| $WS_2/MoTe_2$ | 15.34 | 0.74 | 69.69 | 3.98 | 7.99 | S15 |
| $MoTe_2$ | 16.00 | 0.69 | 65.64 | 25.97 | 7.25 | S16 |
| ***1T'- & $T_d$*-$Mo_{0.66}W_{0.32}Te_{2.02}$** | **16.29** | **0.788** | **73** | **0.62** | **9.40** | **This work** |

In **Table S3**, the photovoltaic parameters of the DSSCs with various TMDs-fabricated CEs were listed to compare with those of a *1T'*- & $T_d$-$Mo_{0.66}W_{0.32}Te_{2.02}$/CC CE-based DSSC. The photovoltaic parameters include short-circuit photocurrent density ($J_{sc}$), open-circuit voltage ($V_{oc}$), fill factor ($FF$), charge-transfer resistance ($R_{ct}$), and power conversion efficiency ($\eta$). All measurements were conducted in the $I_3^-/I^-$ redox couple with N719 photosensitizer dye. As can be seen in the Table, the *1T'*- & $T_d$-$Mo_{0.66}W_{0.32}Te_{2.02}$/CC CE-based DSSC possesses small charge-transfer resistance to enhance the efficiency of 9.4% (despite slightly less than 9.87% of the $CoSe_2$/C hybrid). The comparative analysis demonstrates that the *1T'*- & $T_d$-$Mo_{0.66}W_{0.32}Te_{2.02}$/CC CE of small charge-transfer resistance can be used in DSSCs to improve electrocatalytic activity.

**References**


S1. Fan, M. S.; Lee, C. P.; Li, C. T.; Huang, Y. J.; Vittal, R.; Ho, K. C. Nitrogen-Doped Graphene/Molybdenum Disulfide Composite as the Electrocatalytic Film for Dye Sensitized Solar Cells. *Electrochim. Acta*, **2016**, *211*, 164–172.

S2. Wu, J.; Yue, G.; Xiao, Y.; Huang, M.; Lin, J.; Fan, L.; Lan, Z.; Lin, J. Y. Glucose Aided Preparation of Tungsten Sulfide/ Multi-Wall Carbon Nanotube Hybrid and Use as Counter Electrode in Dye-Sensitized Solar Cells. *ACS Appl. Mater. Interface*, **2012**, *4*, 6530–6536.

S3. Meng, X.; Yu, C.; Lu, B.; Yang, J.; Qiu, J.; Dual Integration System Endowing Two-Dimensional Titanium Disulfide with Enhanced Triiodide Reduction Performance in Dye-Sensitized Solar Cells. *Nano Energy*, **2016**, *22*, 59–69.

S4. Li, Z.; Gong, F.; Zhou, G.; Wang, Z. S. $NiS_2$/Reduced Graphene Oxide Nanocomposites for Efficient Dye-Sensitized Solar Cells. *J. Phys. Chem. C*, **2013**, *117*, 6561– 6566.

S5. Shukla, S.; Loc, N. H.; Boix, P. P.; Koh, T. M.; Prabhakar, R. R.; Mulmudi, H. K.; Zhang, J.; Chen, S.; Ng, C. F.; Huan, C. H. A.; Mathews, N. Iron Pyrite Thin Film Counter Electrodes for Dye-Sensitized Solar Cells: High Efficiency for Iodine and Cobalt Redox Electrolyte Cells. *ACS Nano.* **2014**, *8*, 10597– 10605.

S6. Jin, J.; Zhang, X.; He, T. Self-Assembled $CoS_2$ Nanocrystal Film as an Efficient Counter Electrode for Dye-Sensitized Solar Cells. *J. Phys. Chem. C*, **2014**, *118*, 24877–24883.

S7. Bai, Y.; Zong, X.; Yu, H.; Chen, Z. G.; Wang, L. Scalable Low-Cost $SnS_2$ Nanosheets as Counter Electrode Building Blocks for Dye-Sensitized Solar Cells. *Chem.–Eur. J.*, **2014**, *20*, 8670–8676.

S8. Lee, L. T. L.; He, J.; Wang, B.; Ma, Y.; Wong, K. Y.; Li, Q.; Xiao, X.; Chen, T. Few-Layer $MoSe_2$ Possessing High Catalytic Activity Towards Iodide/Tri-Iodide Redox Shuttles. *Sci. Rep.*, **2014**, *4*, 4063–4069.

S9. Guo, J.; Shi, Y.; Zhu, C.; Wang, L.; Wang, N.; Ma, T. Cost Effective and Morphology-Controllable Niobium Diselenides for Highly Efficient Counter Electrodes of Dye Sensitized Solar Cells. *J. Mater. Chem. A*, **2013**, *1*, 11874–11879.

S10. Guo, J.; Liang, S.; Shi, Y.; Hao, C.; Wang, X.; Ma, T. Transition Metal Selenides as Efficient Counter-Electrode Materials for Dye-Sensitized Solar Cells. *Phys. Chem. Chem. Phys.*, **2015**, *17*, 28985–28992.

S11. Gong, F.; Xu, X.; Li, Z.; Zhou, G.; Wang, Z. S. $NiSe_2$ as an Efficient Electrocatalyst for a Pt-Free Counter Electrode of Dye-Sensitized Solar Cells. *Chem. Commun.*, **2013**, *49*, 1437–1439.

S12. Huang, S.; He, Q.; Chen, W.; Zai, J.; Qiao, Q.; Qian, X. 3D Hierarchical $FeSe_2$ Microspheres: Controlled Synthesis and Applications in Dye-Sensitized Solar Cells. *Nano Energy*, **2015**, *15*, 205–215.

S13. Chiu, I. T.; Li, C. T.; Lee, C. P.; Chen, P. Y.; Tseng, Y. H.; Vittal, R.; Ho, K. C. Nanoclimbing-Wall-Like $CoSe_2$/ Carbon Composite Film for the Counter Electrode of a Highly Efficient Dye-Sensitized Solar Cell: A Study on the Morphology Control. *Nano Energy*, **2016**, *22*, 594–606.

S14. Zhu, L.; Cho, K. Y.; Oh, W. C. Microwave-Assisted Synthesis of $Bi_2Se_3$/Reduced Graphene Oxide Nanocomposite as Efficient Catalytic Counter Electrode for Dye-Sensitized Solar Cell. *Fullerenes, Nanotubes, Carbon Nanostruct.*, **2016**, *24*, 622–629.

S15. Hussain, S.; Patil, S. A.; Memon, A. A.; Vikraman, D.; Abbas, H. G.; Jeong, S. H.; Kim, H.-S.; Kim, H.-S.; Jung, J. Development of a $WS_2$/$MoTe_2$ Heterostructure as a Counter Electrode for the Improved Performance in Dye-Sensitized Solar Cells. *Inorg. Chem. Front.* **2018**, *5*, 3178-3183.

S16. Hussain, S.; Patil, S. A.; Vikraman, D.; Mengal, N.; Liu, H.; Song, W.; An, K.-S.; Jeong, S. H.; Kim, H.-S.; Jung, J. Large Area Growth of $MoTe_2$ Films as High Performance Counter Electrodes for Dye-Sensitized Solar Cells. *Sci. Rep.* **2018**, *8*, 29.